Korean J. Chem. Eng., 33(7), 2169-2178 (2016)
DOI: 10.1007/s11814-016-0076-8

pISSN: 0256-1115
eISSN: 1975-7220

Computational fluid dynamics simulation and particle image velocimetry experimentation of hydrodynamic performance of flat-sheet membrane bioreactor equipped with micro-channel turbulence promoters with micro-pores

Fang Xie, Jinrong Liu†, Jianmin Wang, and Weiwei Chen

School of Chemical Engineering, Inner Mongolia University of Technology, Hohhot, China
(*Received 16 September 2015 • accepted 10 March 2016*)

Abstract−We propose a new type of micro-channel turbulence promoter with micro-pores (MCTP-MPs) which is configured on the flat-sheet membrane surface to decrease membrane fouling and reduce energy consumption. The computational fluid dynamics (CFD) simulation and particle image velocimetry (PIV) experiment are employed to predict turbulent flow in a flat-sheet membrane channel equipped with MCTP-MPs. Velocity profiles and wall shear stresses on membrane surface obtained from PIV were compared with the simulated data to validate the reliability of the CFD simulation. The CFD simulation results and PIV experiment results showed that the corrugated MCTP of 300 μm micro-pores crosswise placed on the membrane surface could increase velocity and wall shear stress on the flat-sheet membrane surface, which improved the filtration flux, reduced concentration polarization and mitigated membrane fouling in the meantime.

Keywords: CFD, Flat-sheet Membrane Bioreactor, Micro-channel Turbulence Promoters with Micro-pores, Membrane Fouling, PIV

INTRODUCTION

Membrane bioreactors are widely applied for the removal of particles, turbidity and microorganisms of wastewater treatment [1]. However, the major obstacles to more widespread applications are membrane fouling and concentration polarization [2-6]. At present, one of the most popular solutions to this problem under much study is to change the state of the fluid flow on the membrane surface so as to control membrane fouling and concentration polarization. Among all the means of changing the state of the fluid flow, the turbulence promoter is the most widely employed because of its simple structure, easy use and good effects of controlling membrane fouling and concentration polarization [7,8].

Turbulence promoters are a different type of barriers which intensify fluid flow state. Zhao et al. [9] conducted microfiltration of yeast fermentation broth with a tubular ceramic membrane equipped with a turbulence promoter and studied the unsteady fluid flow state to alleviate ceramic membrane fouling. In their experiment, there were turbulence promoters of three different structures: helical, winding and with variable cross-section. Tong et al. [10] used turbulence promoters (cylindrical inserts, helical inserts and winding inserts) with backwashing to enhance performance of ceramic membranes for microfiltration of wastewater containing fine TiO_2 particles. The experimental results showed that the flux was increased and energy consumption was reduced. Cao et al. [11] documented that three transverse filament arrangements were simulated with the commercial finite volume package FLUENT to visualize the flow pattern in a rectangular channel. Xu et al. [12,13] were probably among the first to propose the application of turbulence promoters of different shapes (cylindrical, helical and winding) for improving the flux of the MBR and addition of turbulence promoters into ceramic membrane bioreactor to reclaim municipal wastewater. Krstić et al. [14,15] and Jokić et al. [16] employed the kinetic static mixer as a turbulence promoter in cross-flow microfiltration to improve the permeate flux and mitigate membrane fouling. Chen et al. [17] studied the effects of three types of external turbulence promoter (propulsive, helical and cylindrical), which were designed to enhance membrane filtration performance of liquid-solid phase submerged membrane reactor. Zhen et al. [18] investigated four kinds of turbulence promoters (cylindrical, helical, winding and with variable cross-section) to improve the membrane filter performance for wastewater from oil fields. Wu et al. [19] adopted turbulence promoters with different configurations and parameters to enhance micro-mixing efficiency in a ceramic membrane reactor. Liu et al. [20] simulated the fluid flow with CFD in baffle-filled membrane tubes in which an array of central or wall baffles were inserted. The simulation results showed that the presence of baffles causes remarkable increases of average velocity and shear stress on the tube wall, which can significantly improve the filtration performance. Ahmed et al. [21,22] investigated the turbulent flow in a tubular membrane channel containing a set of baffles by CFD simulation. The simulation results indicated that the presence of baffles can improve the local shear stress on the membrane surface, producing eddy activities which enhance filtration performance. Amini et al. [23] documented the CFD simulation of two- and three-phase flows in a flat-sheet submerged membrane module. The CFD results indicated that the cross-flow velocity is a necessary factor to mitigate membrane fouling. Ndi-

†To whom correspondence should be addressed.
E-mail: jinrong_liu@126.com

nisa et al. [24] revealed that flux enhancement was primarily due to an increase in the overall shear stress on the membrane and to more turbulence generated by introduction of the gas phase using CFD simulations. Sengur et al. [25] summarized both effective design and optimized parameters of submerged MBRs using flat-sheet and hollow fiber membranes considering the CFD studies. Um et al. [26] predicted the performance of various designs of a bioreactor and identified the flow pattern and related phenomena in the bench scale tank with CFD model. The results showed that there is a potential for slow or stagnant flow between top impellers and bottom of the tank region and the axial velocity was significantly improved for the modified geometry in the bottom of the tank. Madaeni et al. [27] investigated cake deposition on various parts of the surface of microfiltration membrane due to fouling using the filtration trials and CFD simulations. This results in lower cake deposition on vital parts to minimize the overall fouling. Gimmelshtein et al. [28] reported a flat membrane demo-model, demonstrating the flow through the spacer between two membranes. Velocity was measured and mixing index was estimated by PIV method. Liu et al. [29] used PIV system and high-speed camera to measure water flow hydrodynamics and air bubble size distribution and movements. Willems et al. [30] studied liquid and liquid-gas flows through spacer filled channels using PIV to provide experimental supports for velocity distributions obtained from available CFD studies. Deng et al. [31] investigated the flow pattern in the annulus by PIV and CFD. Both the experimental and simulation results showed that the presence of vertical baffles influences the vertical positions of vortices. Giridharan et al. [32] evaluated the design of a new single port, valve-less counter pulsation device using PIV and CFD. Zhang et al. [33] employed PIV system and a high-speed camera to quantify the liquid flow fields and relative motions between sludge particles and biogas bubbles. Yan et al. [34] discussed the hydrodynamics in a bench-scale airlift flat-sheet MBR with various baffle sizes and locations by CFD simulation and PIV experimentation. The results indicated that baffle location and size were found to have significant effects on MBR hydrodynamics at lower aeration intensities. Xie et al. [35,36] investigated the fouling characteristics and enhancement mechanism of micro-channel turbulence promoters in the submerged flat-sheet membrane bioreactor by CFD simulation and filtration performance experiments. The results showed that the use of an array of corrugated MCTP-MPs in SMBR caused frequent changes in flow directions and generated small eddies and a velocity gradient in the vicinity of the corrugated protrusions.

It follows from the previous work that turbulence promoters can enhance membrane flux and reduce membrane fouling and

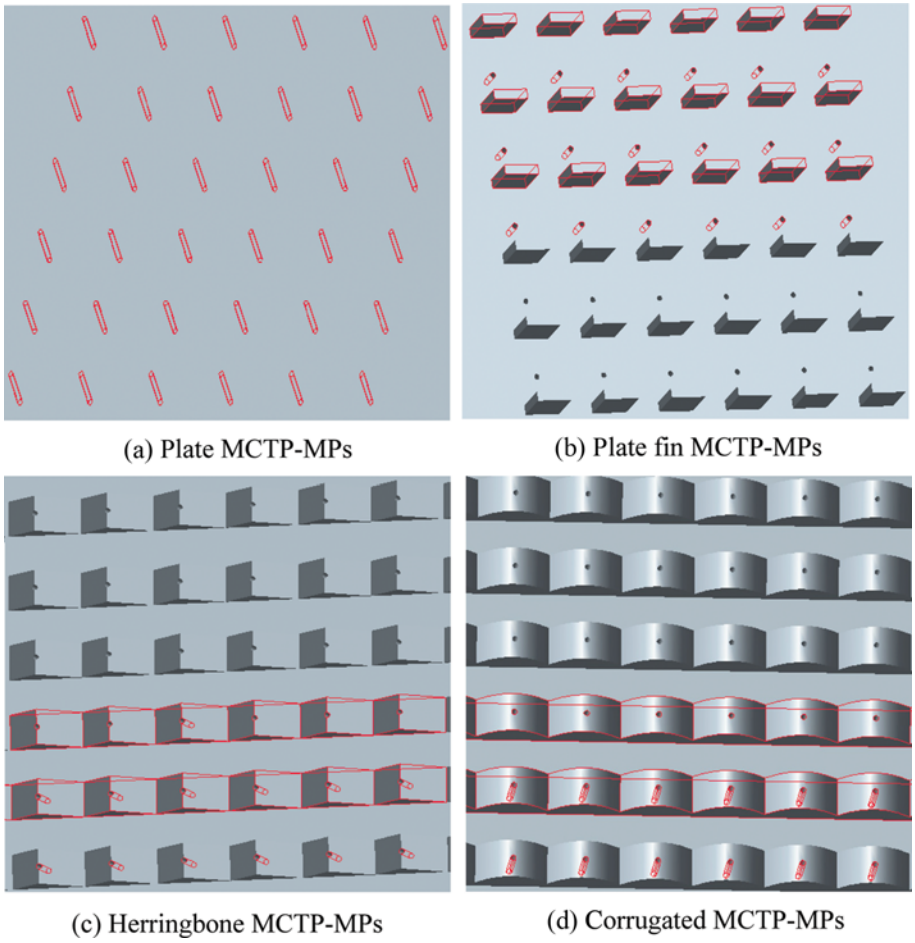

Fig. 1. Schematic diagram of the four types of MCTP-MPs.

concentration polarization, and that CFD can predict the flow pattern and PIV can measure velocity profiles on the membrane surface. The object of this research was to compare the effects of various geometries of a new type of micro-channel turbulence promoter with micro-pores in three kinds of MCTP-MPs locations in the flat-sheet MBR. The optimized results of MCTP-MPs were obtained on the basis of distribution of velocity, turbulent kinetic energy, turbulent dissipate rate, turbulent intensity and wall shear stress. Additionally, the reliability of CFD simulation results was also confirmed by velocity profile and shear stress based on PIV.

METHODS

1. CFD Model

A schematic diagram of the four kinds of MCTP-MPs of different shapes is illustrated in Fig. 1. The width, length and thickness of the micro-channel turbulence promoter are 6 mm, 220 mm and 3 mm, respectively. The width and depth of micro-channel are 1 mm and 2 mm, respectively. The distance between micro-pore and micro-pore is 4 mm. The MCTP-MPs are made of acrylic glass. As the MCTP-MPs and flat-sheet membrane was oriented transverse the flow main flow direction. These two-dimensional calculations are an excellent viewing device for future estimation of more complex MCTP-MPs geometries. The 2D computational flow domain used in this study was a rectangle channel with a width of 72 mm and a length of 320 mm, as shown in Fig. 2(a). The channel geometry was conducted using Meshing of ANSYS 13.0. To ensure an accurate flow in the boundary layer, and the simulation results are closer to the actual flow states, some algorithms on unstructured quad and pave grids are presented for solving the Euler equations. There are individual pores in the micro-channel turbulence promoters. Moreover, MCTP-MPs is only localized in the membrane channel; therefore, a unified approach is adopted in CFD simulation. The finer computational grids have been employed in the MCTP-MPs and flat-sheet membrane by defining the fixed size function, where high gradients of velocity and wall shear stress may exist [21]. Five grid sizes of different types were used in the simulations to obtain a grid independent solution. The results are shown in Table 1. It can be found that 126,417 cells obtain a grid independent solution.

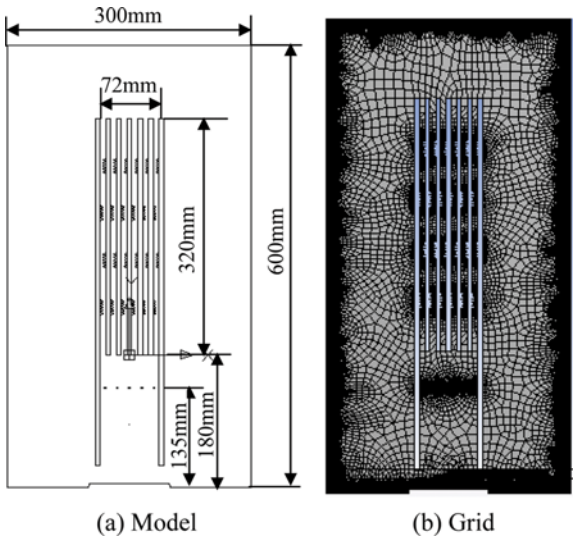

Fig. 2. Geometric model and grid generation.

Table 1. Grid independence data

Case number	Grid size	Average velocity (m s^{-1})
1	89,575	0.71
2	104,814	0.76
3	116,643	0.79
4	126,417	0.80
5	131,852	0.80

2. Turbulence Model

In this study, the standard k-epsilon model and wall functions [37] were used to perform CFD simulations. In the CFD simulations, it was assumed that the fluid was incompressible, with constant physical properties and steady turbulent state flow. Under these assumptions, the standard k-epsilon model turbulent kinetic energy (k) and turbulent dissipate rate (ε) are the two basic unknown quantities, whose transport equations [38] are as follows:

$$\frac{\partial(\rho k)}{\partial t}+\frac{\partial(\rho k u_i)}{\partial x_i}=\frac{\partial}{\partial x_j}\left[\left(u+\frac{u_i}{\sigma_k}\right)\frac{\partial k}{\partial x_j}\right]+G_k-\rho\varepsilon \quad (1)$$

$$\frac{\partial(\rho\varepsilon)}{\partial t}+\frac{\partial(\rho\varepsilon u_i)}{\partial x_i}=\frac{\partial}{\partial x_j}\left[\left(u+\frac{u_i}{\sigma_\varepsilon}\right)\frac{\partial\varepsilon}{\partial x_j}\right]+C_{1\varepsilon}\frac{\varepsilon}{k}G_K-C_{2\varepsilon}\rho\frac{\varepsilon^2}{k} \quad (2)$$

where, ρ (kg m^{-3}) is the density, u the velocity (m s^{-1}), μ the viscosity (Pa s), G_k the turbulent kinetic energy caused by the average velocity gradient, $C_{1\varepsilon}$=1.44, $C_{2\varepsilon}$=1.92, δ_k=1.0, and δ_z=1.3.

Wall functions are expressed as:

$$G_k\approx\tau_w\frac{\partial u}{\partial y}\approx\tau_w\frac{\tau_w}{\kappa\rho C_\mu^{1/4}k_p^{1/2}\Delta y_p} \quad (3)$$

$$\varepsilon=\frac{C_\mu^{3/4}k_p^{3/2}}{\kappa\Delta y_p} \quad (4)$$

where, τ_w is wall shear stress (Pa), Δy the distance from point P to the wall (m), κ=0.42, C_μ=0.09, and k_p the turbulent kinetic energy at point P (m^2 s^{-2}).

3. Solution Approach and Boundary Conditions

The CFD code (Fluent 13.0), which employs the finite volume method, is used to simulate the hydrodynamic characterization in the channel between micro-channel turbulence promoters and flat-sheet membrane. The computational domain was discretized by a second-order upwind differencing scheme. The pressure-velocity coupling scheme was resolved with SIMPLE algorithm. The scaled residuals were monitored to a criterion of 10^{-5} for the continuity and momentum variables as well as k-epsilon to ensure the convergence of the numerical solution. The fluid flow in the membrane channel without turbulence promoters (NTP) was also simulated for the purpose of comparison. The boundary conditions used here are identical for all cases of these simulations, with an inlet velocity of 0.5 m s^{-1} and the outlet set as outflow. The flat membrane and micro-channel turbulence promoters were assumed to be the wall boundary condition was set for them because per-

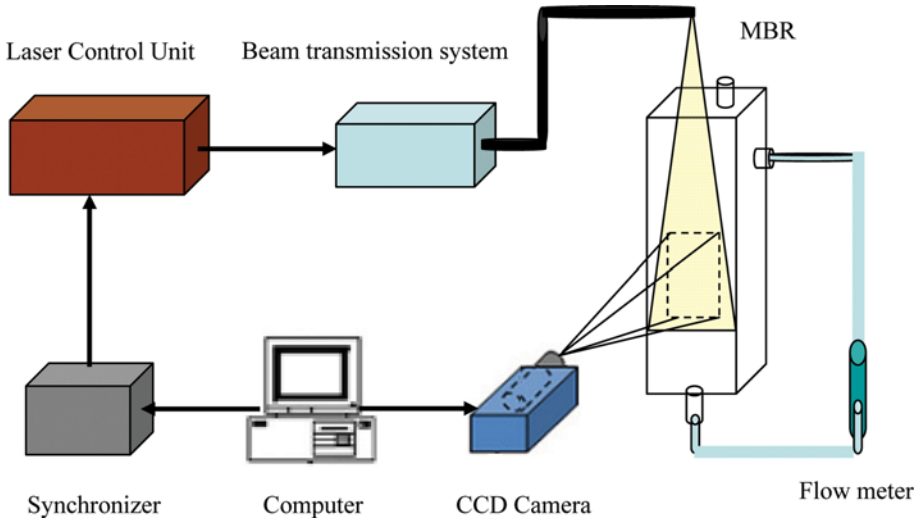

Fig. 3. Schematics diagram of the PIV setup for experiments.

meate extraction is negligible against the total flow in the system [23]. The wall boundary condition equation is as follows:

$$\frac{u}{u_\tau} = \frac{\rho u_\tau y}{\mu} \quad (5)$$

where, u is the velocity parallel to the wall, u_τ the shear velocity, y the distance from the wall, ρ (kg m^{-3}) the density, and μ the viscosity (Pa s).

4. PIV Experiments

Velocity profiles and wall shear stresses on membrane surface obtained from PIV (USA TSI, Power View, 3DPIV) were compared with simulated data to validate the reliability of the CFD results. Because the flat-sheet membrane is not a transparent body, the membrane bioreactor is vertically illuminated in a flow field with laser sheets by the laser arm (Big Sky laser, wavelength 545-780 nm, single pulse energy 120 MJ) above the top of membrane bioreactor system to capture images of the tracer particles at a certain time interval. CCD camera system (resolution 1200×1600, 16 fps) was placed in the front of the membrane reactor. A synchronizer controlled the laser system and the camera system. Image acquisition software (Insight3G) collected images from CCD and got the flow field distribution on the image area required. Tecplot10 is post-processing software for the velocity field of Insight3G. More detailed information about the PIV system setup is presented in Fig. 3. The tracer particles by experiment were micro glass beads, with particle size 15 μm.

RESULTS AND DISCUSSION

1. Effect of Different Shapes of Turbulence Promoters

1-1. Contours of Velocity Magnitude

Velocity distribution indicates fluid flow states between plate MCTPs, herringbone MCTP-MPs, corrugated MCTP-MPs, plate fin MCTP-MPs and the flat-sheet membrane channel are illustrated in Fig. 4 and Fig. 5. The lower the velocity is, the easier the particles in the feed suspension deposit on the membrane surface to form a thick cake layer, which results in the decline of filtration

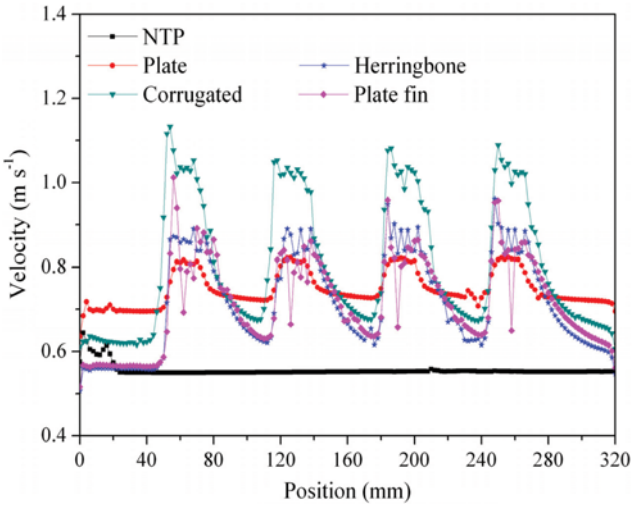

Fig. 4. Velocity distribution along the flat-sheet membrane length.

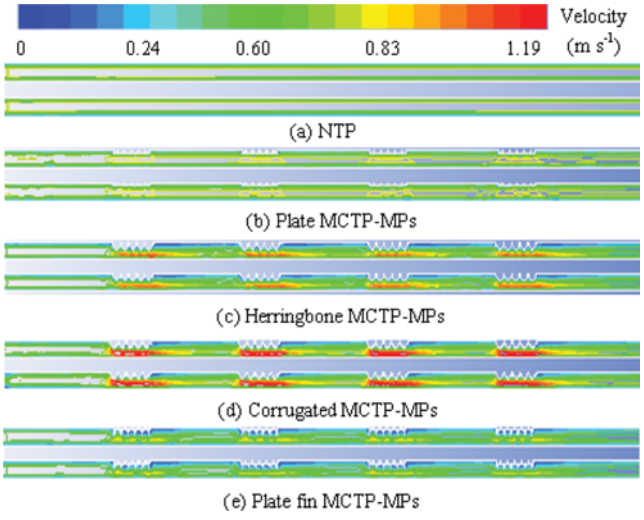

Fig. 5. Contours of velocity magnitude along the membrane channel.

flux [13,20,21]. It is clear that the velocity of the flat-sheet membrane channel equipped with MCTP-MPs is higher than that of the flat-sheet membrane channel without TP. Moreover, there is no eddy formation and velocity fluctuation of the flat-sheet membrane channel without TP; however, all channels between the flat-sheet membrane and MCTP-MPs have eddy formations and velocity fluctuation. As to the corrugated MCTP-MPs, the trough and peak values of wall velocities are about 0.65 m s^{-1} and 1.19 m s^{-1}, respectively. High velocity, eddy formation and velocity fluctuation not only increase turbulence in the bulk fluid stream but also interrupt the buildup of the boundary layer and disturb the development of concentration polarization layer on the membrane surface, which contributes to reducing membrane fouling and improving filter performance of the membrane.

1-2. Turbulence Characteristic

1-2-1. Turbulent Kinetic Energy and Turbulent Dissipation Rate

The presence of an array of turbulence promoters in the flat-sheet membrane channel causes frequent changes of flow directions and the intense velocity fluctuations, which leads to higher flow turbulence [20,35,36]. The distributions of turbulent kinetic energy and its dissipation rate along the length of membrane channel are shown in Fig. 6 and Fig. 7, respectively.

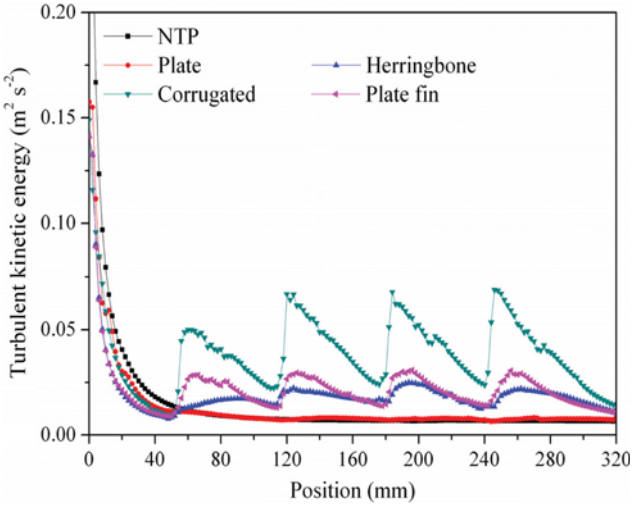

Fig. 6. Turbulent kinetic energy distribution along the length of membrane channel.

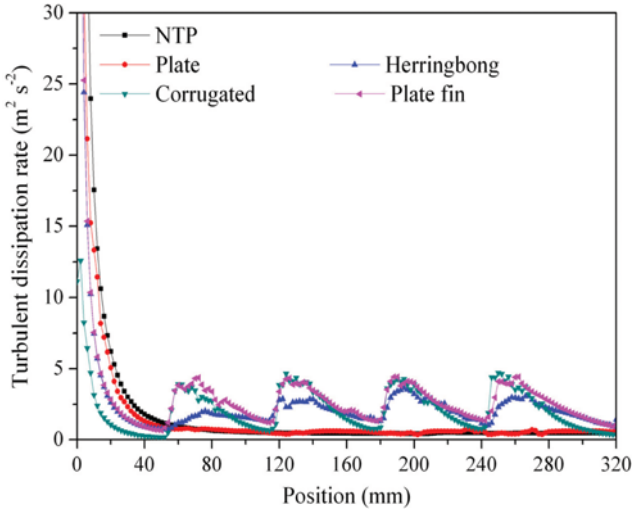

Fig. 7. Turbulent dissipation rate distribution along the length of membrane channel.

It can be observed that the turbulent kinetic energy and turbulent dissipation rate for liquid flow in the membrane channel with plate fin MCTP-MPs and corrugated MCTP-MPs are higher than those of the others. Compared with the membrane channel without TP, the membrane channel with MCTP-MPs can produce higher turbulent kinetic energy, which means that the fluid flow can retain higher turbulence along the membrane channel, thus disrupting the concentration of the boundary layer and decreasing particle deposition on the membrane surface. Therefore, membrane fouling and concentration polarization can be effectively controlled. Moreover, the higher turbulent dissipation rate is, the higher pressure drop is in the membrane module due to turbulent energy dissipation.

1-2-2. Turbulent Intensity

Turbulent kinetic energy is one of the most important variables of the boundary layer since it is a measure of turbulent intensity. The turbulence intensity, also often known as the turbulence level, is set as the ratio of square root mean of the turbulent velocity fluctuations to the average velocity [35]. The distributions of turbulent intensity along the membrane channel are shown in Fig. 8. In contrast to the membrane channel without TP, the membrane with MCTP-MPs can produce higher turbulent intensity. The average turbulent intensity of the corrugated MCTP-MPs is 31.23%, which indicates higher level of turbulence. This means that the concentration boundary layer is disrupted and the particle deposition upon the membrane surface is decreased, therefore, membrane fouling can be effectively controlled.

1-3. Static Pressure

The distribution of static pressure along the membrane length is depicted in Fig. 9. For the four types of turbulence promoters, a sudden drop of static pressure along the flat-sheet membrane channel with turbulence promoters is an unavoidable phenomenon, corre-

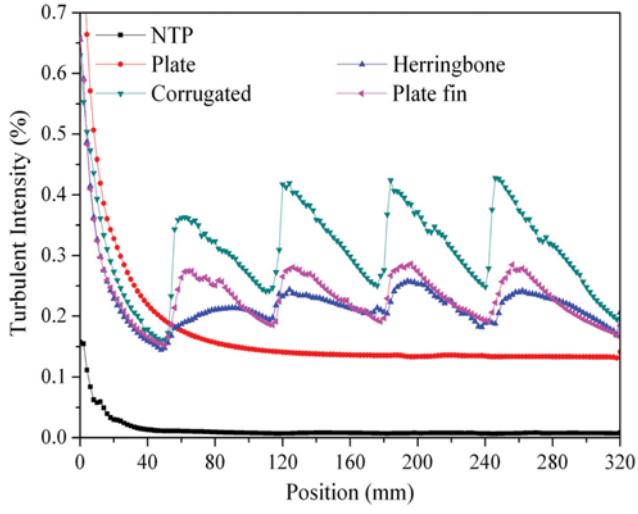

Fig. 8. Turbulent intensity distribution along the length of membrane channel.

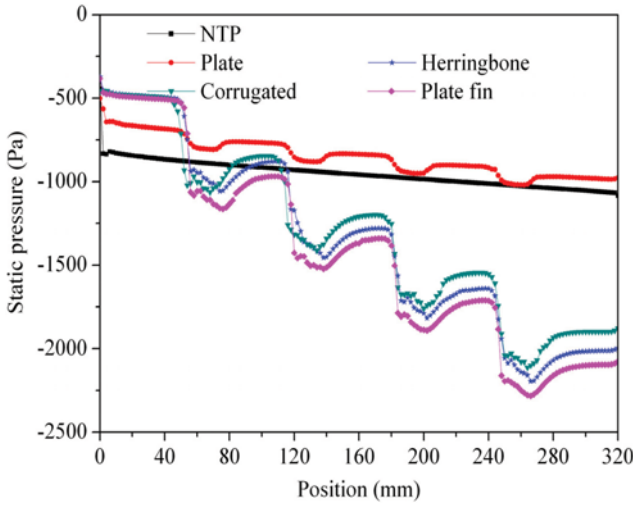

Fig. 9. Static pressure distribution along the length of membrane channel.

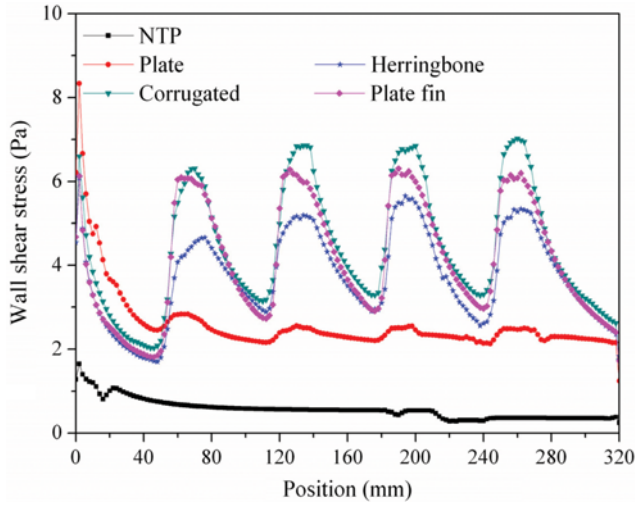

Fig. 10. Wall shear stress distribution on the membrane surface.

sponding to the fluctuation of velocity magnitude and eddy formation.

In Fig. 9, the value of pressure drop along the flat-sheet membrane channel can be obtained from the difference of static pressure between the inlet (x=0 m) and the outlet (x=320 mm). It can be shown that the pressure drop increases faster along the membrane channel with MCTP-MPs than that along the membrane channel without TP. The pressure drops along the channel are about 1.82 kPa, 1.86 kPa, 1.42 kPa for the membrane channels with herringbone MCTP-MPs, plate fin MCTP-MPs, and corrugated MCTP-MPs, respectively, which are higher than that for the membrane channel without TP (0.52 kPa). The greater the pressure drop is, the higher the energy cost of the membrane module. So the energy consumption for the membrane with plate fin MCTP-MPs is the highest. The reasons for higher pressure drops along the flat-sheet membrane channel with MCTP-MPs could be interpreted as follows. First, the use of an array of turbulence promoters in the flat-sheet membrane channel causes frequent changes of flow directions and intense velocity fluctuations. Secondly, eddies formed also lead to the increase of energy loss because of turbulent energy dissipation [20-22].

1-4. Wall Shear Stress

The wall shear stress (τ_w) is given by:

$$\tau_w = \mu\left(\frac{\partial u}{\partial y}\right)_{y=0} \tag{9}$$

where, μ is the dynamic viscosity, u is the flow velocity parallel to the wall and y is the vertical distance to the wall. From Fig. 4 and Fig. 10, the fluctuation of velocity can result in the fluctuation of wall shear stress. For all membrane channels with MCTP-MPs, the wall shear stress is higher than that of membrane channels without TPs. As to plate fin MCTP-MPs, the peak and trough values of wall shear stress are about 6.5 Pa and 1.8 Pa, respectively, and the average value is more than 4 Pa. For the corrugated MCTP-MPs, the peak and trough values of wall shear stress are about 7 Pa and 2 Pa respectively, and the average value is more than 5 Pa. Without TP, the highest value of wall shear stress is below 2 Pa and the average value is about 1.5 Pa. The higher wall shear stress is, the easer molecular diffusion is, which inhibits the buildup of the cake layer on the membrane surface and reduces concentration polarization.

From the above analysis, it can be seen that the hydrodynamic performance of the membrane channel equipped with MCTP-MPs is better than that of the membrane channel without TP, and the hydrodynamic performance of the membrane channel with corrugated MCTP-MPs is the best. So, the membrane channel with corrugated MCTP-MPs is selected for the following simulation.

2. Effect of Different Micro-pore Sizes of Micro-channel Turbulence Promoters

The micro-pores of micro-channel turbulence promoters cause changes of hydrodynamic performances of the membrane channel and surface. Micro-pore sizes (diameter) of 100 μm, 200 μm, 300 μm, 400 μm and 500 μm are simulated by CFD. From Fig. 11, it is evident that the average value of the velocity increases with the micro-pore size (≤300 μm) increase; however, the velocity decreases with the micro-pore diameter when the micro-pore diameter is above 300 μm due to the characteristic of micro-channel turbulence promoters. In the micro-channel, the velocity gradient increases

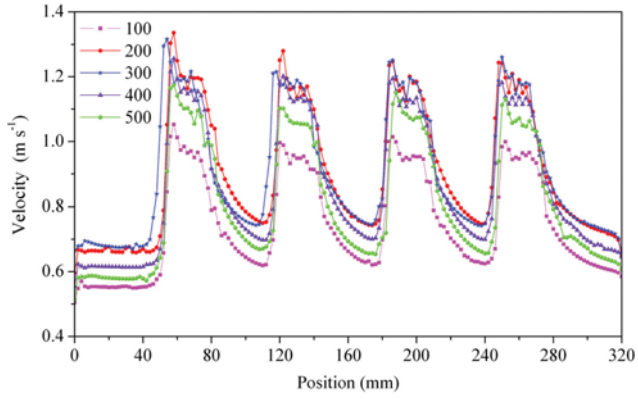

Fig. 11. Effect of micro-pore size on velocity.

with the decreasing of e scale; however, the micro-pore in micro-channel turbulence promoters is so small not to be a benefit of increasing velocity because of being similar to plate micro-channel turbulence promoters [36]. Likewise, a similar trend is observed for the turbulent kinetic energy and wall shear stress as indicated in Fig. 12 and Fig. 13. The increase of velocity, turbulent kinetic energy and wall shear stress is valuable for improving the filtration flux and reducing the membrane fouling. It can be seen clearly in Fig. 14 that micro-pore size has little effect on the pressure drop, which is associated with the energy consumption.

3. Effect of Different Positions of Turbulence Promoters in the MBR

To increase flux and improve membrane filtration performance,

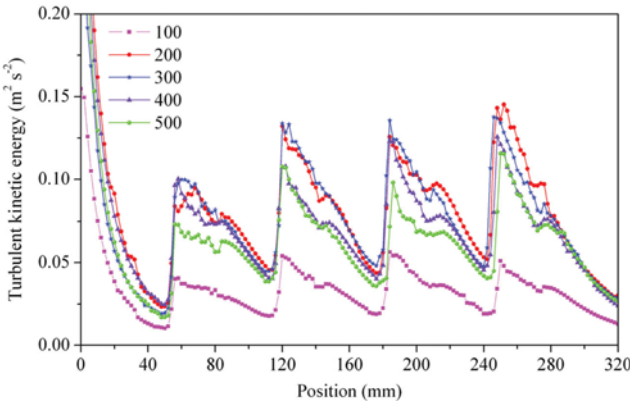

Fig. 12. Effect of micro-pore size on turbulent kinetic energy.

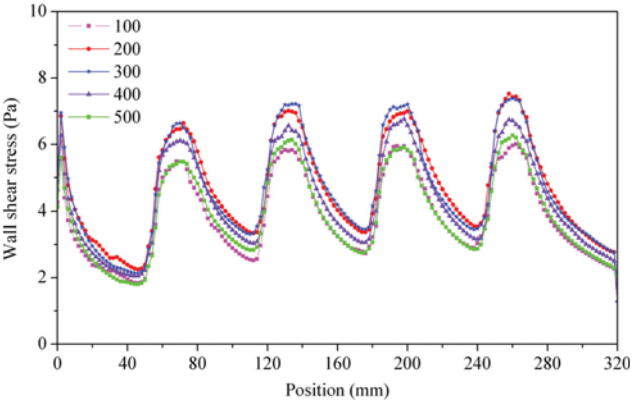

Fig. 13. Effect of micro-pore size on wall shear stress.

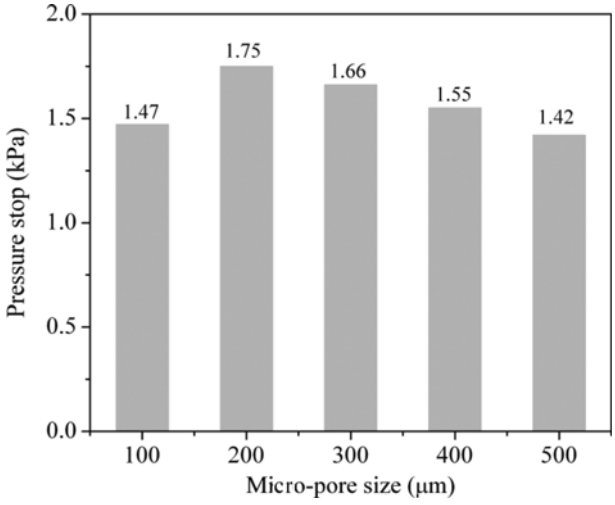

Fig. 14. Effect of micro-pore size on pressure drop.

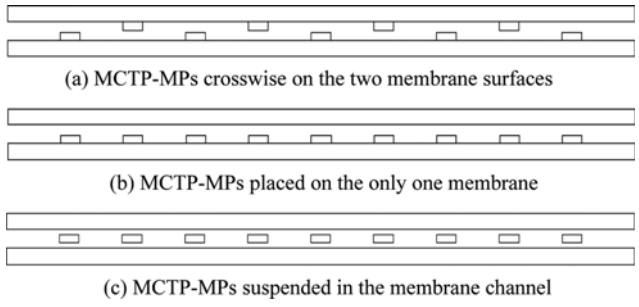

Fig. 15. Schematic diagram of MCTP-MPs position in the MBR.

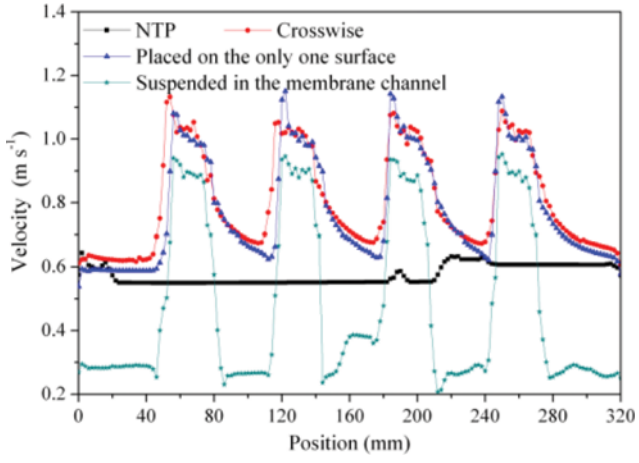

Fig. 16. Effect of different position of MCTP-MPs on velocity.

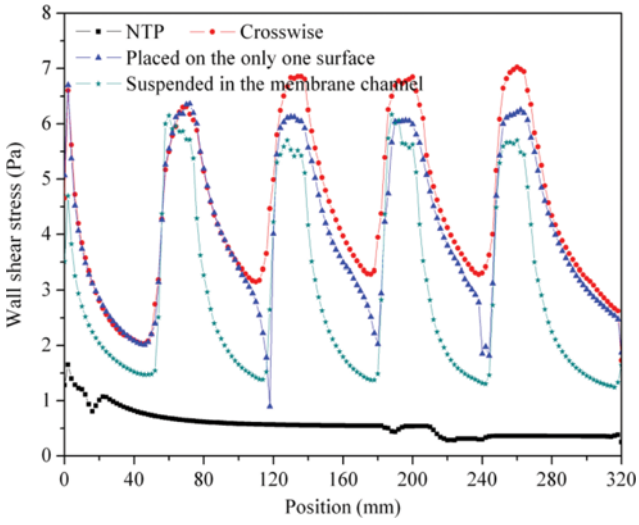

Fig. 17. Effect of different position of MCTP-MPs on wall shear stress.

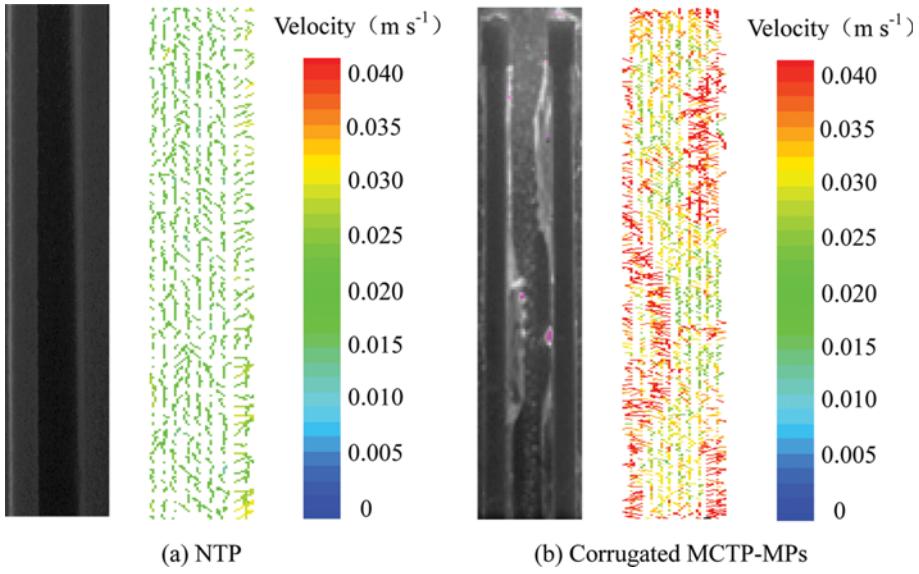

Fig. 18. PIV image and velocity profiles of NTP and corrugated MCTP-MPs.

MCTP-MPs position in the MBR should be given great consideration. Turbulence promoters placed in different positions in flat-sheet membrane channels are illustrated in Fig. 15.

Velocity distribution along the channel is depicted in Fig. 16, where it can be seen that flow directions undergo sudden changes and eddies are formed through the membrane channel with MCTP-MPs crosswise placed on membrane surfaces. Fig. 17 shows that the peak and trough of the wall shear stress are dependent on velocity magnitude. The wall shear stress of MCTP-MPs crosswise placed on the membrane surface is greater than that of the others. From above analysis, MCTP-MPs placed crosswise on the membrane surface is the optimum.

4. Experimental Validation of CFD Simulation

The velocity profiles and wall shear stresses on the flat-sheet membrane surface are measured by PIV and compared with the optimum CFD simulation results. It is observed from Fig. 18 that the corrugated MCTP of 300 μm micro-pores crosswise placed on the membrane surface not only causes velocity fluctuations and eddy formations, but also increases velocities on the membrane surface, especially in the vicinity of MCTP-MPs.

There are many tracer particles which are the micro glass beads of 15 μm in the flow field. The pulse laser sheets illuminated a flow field with two consecutive exposures to capture images of the tracer particles at a certain time interval by CCD and other imaging equipments. We recorded the time interval between adjacent two frames and analyzed the two consecutive PIV image, therefore identified the displacement of trace particles and obtained the velocity vector of each point, moreover, calculated the other parameters [39]. The schematic diagram of PIV testing principle is illustrated in Fig. 19. Velocity and wall shear stress are measured along

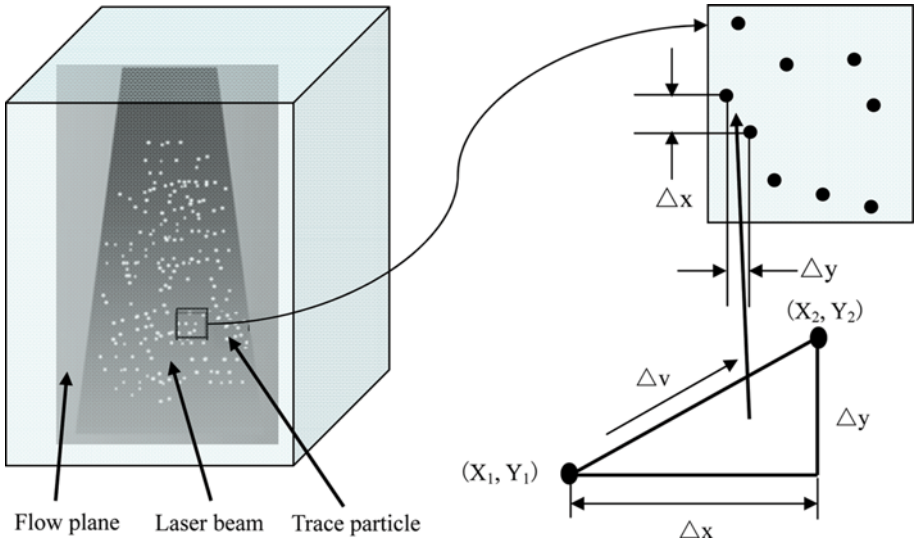

Fig. 19. The schematic diagram of PIV testing principle.

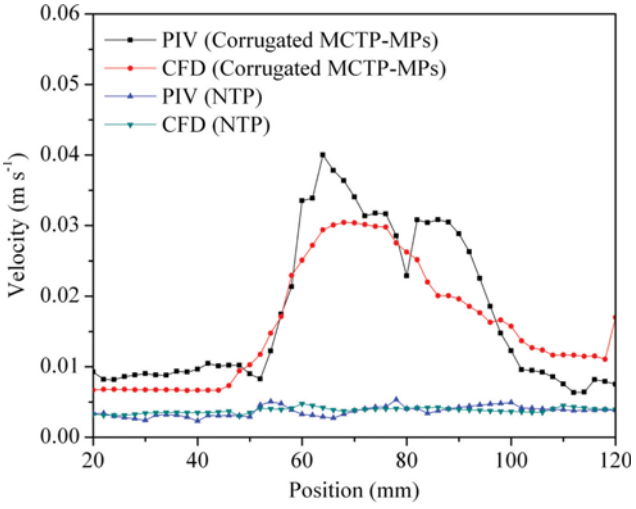

Fig. 20. Velocity on the membrane surface by PIV and CFD.

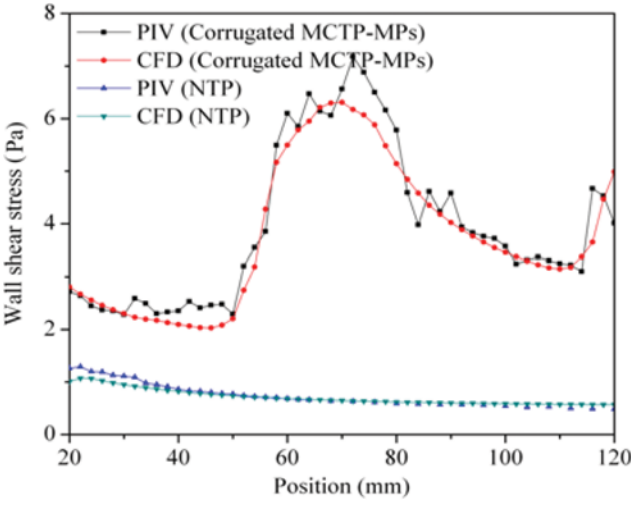

Fig. 21. Wall shear stress on the membrane surface by PIV and CFD.

the line of x=[20, 120] mm, y=6 mm. It is known from Fig. 20 and Fig. 21 that PIV experiment results are similar to the CFD simulation results, with average errors of 2.97% and 4.42%, which are obtained according to Eqs. (5) and (6). This proves that the turbulence and single phase models were chosen appropriately in the CFD package and the meshes generated have satisfactory quality to give reliable simulations of the reality of hydrodynamics in this study.

$$E_v = \frac{\overline{v}_{CFD} - \overline{v}_{PIV}}{\overline{v}_{CFD}} \times 100\% \quad (6)$$

$$E_{\tau_w} = \frac{\overline{\tau}_{wCFD} - \overline{\tau}_{wPIV}}{\overline{\tau}_{wCFD}} \times 100\% \quad (7)$$

where, E_v - the error of velocity, E_{τ_w} - the error of wall shear stress, $\overline{v}_{CFD}$, $\overline{\tau}_{wCFD}$ - average velocity and wall shear stress of CFD simulation, $\overline{v}_{PIV}$, $\overline{\tau}_{wPIV}$ - average velocity and wall shear stress of PIV experiment.

CONCLUSIONS

The effects of MCTP-MPs in four different shapes, with five different sizes of micro-pores and three different positions in the MBR on hydrodynamic performance were investigated through CFD. The simulation results reveal the detailed flow pattern, velocity, turbulence characteristics, static pressure and wall shear stress. It is found that MCTP-MPs not only cause velocity fluctuation and eddy formation, but also increase wall shear stress on the membrane surface. By comparing simulation results, the shape of turbulence promoter, the position in the membrane channel and the size of micro-pores are all very important to the performance of MBR. The corrugated MCTP of 300 μm micro-pore crosswise placed on the membrane surface can increase wall shear stress on the flat-sheet membrane surface and turbulent kinetic energy along the membrane channel, improving filtration performance while reducing membrane fouling and concentration polarization in the meantime. Also, CFD simulation and PIV experiment results indicate that the corrugated MCTP-MPs can improve the filtration flux and save energy consumption compared with the others. However, to achieve minimum energy consumption while reducing the concentration polarization and membrane fouling, optimum geometry design of the corrugated MCTP-MPs should be further evaluated. In follow-up studies, the filtration performance and membrane fouling resistance experiment of flat-sheet membrane bioreactor were investigated to validate CFD simulation results. Furthermore, the development of strategies for MCTP-MPs used to control membrane fouling and enhance flux in MBR can be further researched.

REFERENCES

1. P. Kanagaraj, S. Neelakandan and A. Nagendran, *Korean J. Chem. Eng.*, **31**(1), 1057 (2014).
2. F. G. Meng and S. R. Chae, *Water Res.*, **43**, 1489 (2009).
3. Z. W. Wang, Z. C. Wu and S. H. Mai, *Sep. Purif. Technol.*, **62**, 249 (2008).
4. W. Stefan and R. Thorsten, *Water Res.*, **42**, 3837 (2008).
5. A. Drews, *J. Membr. Sci.*, **363**(1-2), 1 (2010).
6. A. Abdelrasoul, H. Doan, A. Lohi and C. H. Cheng, *Korean J. Chem. Eng.*, **33**(3), 1014 (2016).
7. Y. F. Liu, G. H. He and B. J. Li, *Ind. Eng. Prog.*, **25**, 30 (2006).
8. W. H. Xing, J. Z. Tong, N. P. Xu and J. Shi, *Chem. Ind. Eng. Prog.*, **1**, 44 (2000).
9. Z. G. Zhao and J. Tao, *Chem. Ind. Eng. Prog.*, **24**, 315 (1997).
10. J. Z. Tong, W. H. Xing, N. P. Xu and J. Shi, *J. Chem. Eng. Chin. Univ.*, **13**, 421 (1999).
11. Z. Cao, D. E. Wiley and A. G. Fane, *J. Membr. Sci.*, **185**, 157 (2001).
12. N. Xu, W. H. Xing, N. P. Xu and J. Shi, *J. Membr. Sci.*, **210**, 307 (2002).
13. N. Xu, W. H. Xing, N. P. Xu and J. Shi, *Sep. Purif. Technol.*, **32**, 403 (2003).
14. D. M. Krstić, M. N. Tekić, M. Đ. Carić and S. D. Milanovic, *Desalination*, **163**, 297 (2004).
15. D. M. Krstić, A. K. Koris and M. N. Tekić, *Desalination*, **191**, 371 (2006).

16. A. Jokić, Z. Zavargo, Z. Šereš and M. Tekić, *J. Membr. Sci.*, **350**, 269 (2010).
17. R. Z. Chen, L. X. Zhang, W. H. Xing and N. P. Xu, *Mod. Chem. Ind.*, **25**, 56 (2005).
18. X. H. Zhen, S. L Yu, B. F. Wang and H. F. Zheng, *J. Membr. Sci.*, **18**, 1077 (2006).
19. Y. Wu, C. Hua, W. L. Li, Q. Li, H. S. Gao and H. Z. Liu, *J. Membr. Sci.*, **328**, 219 (2009).
20. Y. F. Liu, G. H. He, X. D. Liu, G. K. Xiao and B. J. Li, *Sep. Purif. Technol.*, **67**, 14 (2009).
21. S. Ahmed, M. T. Seraji, J. Jahedi and M. A. Hashib, *Desalination*, **278**, 191 (2011).
22. S. Ahmed, M. T. Seraji, J. Jahedia and M. A. Hashibb, *Chem. Eng. Res. Des.*, **90**, 600 (2012).
23. E. Amini, M. R. Mehrnia, S. M. Mousavi and N. Mostoufi, *Ind. Eng. Chem. Res.*, **52**, 9930 (2013).
24. N. V. Ndinisa, A. G. Fane, D. E. Wiley and D. F. Fletcher, *Sep. Sci. Technol.*, **41**, 1411 (2006).
25. R. Sengur, G. Deveci, R. Kaya, T. Turken, S. Guclu, D. Y. Imer and I. Koyuncu, *Desalin. Water Treat.*, **55**(7), 1747 (2015).
26. B. H. Um and T. R. Hanley, *Korean J. Chem. Eng.*, **25**(5), 1094 (2008).
27. S. S. Madaeni, M. Rahimi and M. Abolhasani, *Korean J. Chem. Eng.*, **27**(1), 206 (2010).
28. M. M. Gimmelshtein and R. Semiat, *J. Membr. Sci.*, **264**, 137 (2005).
29. N. Y. Liu, Q. D. Zhang, G. L. Chin, E. H. Ong, J. Lou, C. W. Kang, W. J. Liu and E. Jordan, *J. Membr. Sci.*, **353**, 122 (2010).
30. P. Willems, N. G. Deen, A. J. B. Kemperman, R. G. H. Lammertink, M. Wessling, M. van Sint Annaland, J. A. M. Kuipers and W. G. J. van der Meer, *J. Membr. Sci.*, **362**, 143 (2010).
31. R. S. Deng, D. Y. Arifin, M. Y. Chyn and C. H. Wang, *Chem. Eng. Sci.*, **65**, 4598 (2010).
32. G. A. Giridharan, C. Lederer, A. Berthe, L. Goubergrits, J. Hutzenlaub, M. S. Slaughter, R. D. Dowling, P. A. Spence and S. C. Koenig, *Med. Eng. Phys.*, **33**, 1193 (2011).
33. J. B. Zhang, S. Poncin, J. Wub and H. Z. Li, *Chem. Eng. Sci.*, **66**, 3423 (2011).
34. X. X. Yan, K. Xiao, S. Liang, T. Lei, P. Liang, T. Xue, K. C. Yu, J. Guan and X. Huang, *Bioresour. Technol.*, **175**, 633 (2015).
35. F. Xie. W. W. Chen, J. M. Wang and J. R. Liu. *J. Membr. Sci.*, **495**, 361 (2015).
36. F. Xie. W. W. Chen, J. M. Wang and J. R. Liu. *Chem. Eng. Process.*, **99**, 72 (2016).
37. F. J. Wang, China Tsinghua University Press (2004).
38. J. L. Li, China Chemistry Industry Pressure (2009).
39. J. Grue, P. L. F. Liu and G. K. Pedersen, World Scientific Publishing Co. Pte Ltd. (2004).